Seventh International Conference on Computational Fluid Dynamics (ICCFD7), Big Island, Hawaii, July 9-13, 2012

ICCFD7-3001

A Hydrothermal Convective Flow at Extremely High Temperature

S. Komurasaki
Corresponding author: satoko@math.cst.nihon-u.ac.jp

College of Science and Technology, Nihon University, Japan.

Abstract: To investigate the flow structure of a hydrothermal convection in the deep sea, a thermal convective flow is simulated, where the temperature of the heated water and the environmental pressure are very high above its critical point. The compressible Navier-Stokes equations are solved using the numerical method similar to an incompressible flow. The equations are discretized based on the multidirectional finite difference method. Numerical results clearly show differences in the flow field depending on the temperature of the heated water. Under conditions close to the critical temperature, the flow is sensitive to the temperature of the heated water. At temperature above the critical temperature, the thermal convection develops faster and the flow structure is extremely complex and unsteady.

Keywords: Hydrothermal Convection, Supercritical Water, Incompressible Flow Computation, Flow Structure.

1 Introduction

Hydrothermal convective flows are found in geothermally heated water issued from hydrothermal vents. They are found in deep oceans of depth over 2,000 m where the hydrostatic pressure is over 20 MPa, and the temperature of the heated water is sometimes over 300°C. Under these conditions, where the pressure and temperature are beyond the critical point, water emerging from these vents can be in a supercritical state that is a condition between a gas and a liquid. Close to the critical point, small changes in pressure or temperature cause large changes in density. However, under the conditions of high constant pressure and low environmental temperature in the deep sea, the density changes principally depending on the temperature, and the heated water issued from the vent is cooled and rapidly becomes liquid. Since supercritical fluids generally have properties between those of a gas and a liquid, properties such as density significantly change during the phase transition to the liquid. Therefore, hydrothermal convection beyond the critical temperature in the deep sea can be regarded as a thermal convection with properties rapidly changing with temperature.

In the present study, to investigate the flow structure of the hydrothermal plumes at extremely high temperature in the deep sea, a simple numerical model is proposed and the flow is simulated. Understanding the mechanism of the complex unsteady flow with large changes in the temperature and other properties, helps to clarify a process of the advection and diffusion of materials which are issued from hydrothermal vents accompanying the heated water. That is important in order to deepen the understanding of the oceanic crust that contains abundant resources. Moreover, it may be useful for understanding the "seafloor hydrothermal circulation" that is the very large-scale water circulation caused by the hydrothermal eruption and absorption of the cold sea water into the seafloor.

2 Computational Method

2.1 The basic equations

The basic equations are derived from the compressible Navier-Stokes equations and the energy equation using the assumption that pressure difference from environmental pressure p_b is sufficiently small and does not affect the density change. And also the flow velocity is assumed to be much smaller than the sound velocity. This means that the density is only a function of temperature. The basic equations in Cartesian coordinates with the x_3-axis in the vertical direction in space, are as follows;

$$\frac{1}{\rho}\frac{D\rho}{Dt} = -\frac{\partial u_j}{\partial x_j} \tag{1}$$

$$\frac{Du_i}{Dt} = -\frac{1}{\rho}\frac{\partial p}{\partial x_i} + \frac{1}{\rho}\frac{\partial}{\partial x_j}\mu\frac{\partial u_i}{\partial x_j} - \boldsymbol{e}_3 g \qquad \boldsymbol{e}_3 = (0,0,1) \tag{2}$$

$$C_v\frac{DT}{Dt} + p\frac{D}{Dt}\left(\frac{1}{\rho}\right) = \frac{1}{\rho}\frac{\partial}{\partial x_j}\kappa\frac{\partial T}{\partial x_j}. \tag{3}$$

The energy equation (3) is obtained using $C_p(DT/Dt) \sim C_v(DT/Dt) + p(D/Dt)(1/\rho)$. Equation for density ρ is derived using an interpolation polynominal of the temperature under constant pressure:

$$\frac{1}{\rho} = a_m T + b_m \qquad (T_m \le T < T_{m+1}) \tag{4}$$

($0 \le m \le M$, $\quad T_0 = T_{min}:$ Temperature of environmental water, $\quad T_M = T_{max}:$ Temperature of heated water.)

Other properties, viscosity μ, thermal conductivity κ and specific heat at constant volume C_v are also functions of the temperature, in the same way as the density.

Using a pressure difference δp from the environmental water pressure p_b that satisfies the hydrostatic equilibrium equation $\partial p_b/\partial x_3 = -\rho_0 g$, pressure gradients in Eq. (2) are rewritten as

$$\frac{\partial p}{\partial x_i} = \frac{\partial \delta p}{\partial x_i} - \boldsymbol{e}_3\rho_0 g \qquad (p = p_b + \delta p) \tag{5}$$

where ρ_0 is the density of environmental water and is a constant. When vertical length scale is small, change in p_b with the depth can be ignored. Here, p_b is assumed to be almost constant at $p_0 = 23$ MPa which is above the critical pressure of 22.064 MPa.

Using Eq. (5) and p_0 instead of p in Eq. (3), the basic equations are rewritten as

$$\tilde{\rho}\frac{D}{D\tilde{t}}\left(\frac{1}{\tilde{\rho}}\right) = \frac{\partial \tilde{u_j}}{\partial \tilde{x_j}} \tag{6}$$

$$\frac{D\tilde{u_i}}{D\tilde{t}} = -\frac{1}{\tilde{\rho}}\frac{\partial \tilde{\delta p}}{\partial \tilde{x_i}} + \frac{1}{\tilde{\rho}}\frac{\partial}{\partial \tilde{x_j}}\frac{1}{\mathrm{Re}}\frac{\partial \tilde{u_i}}{\partial \tilde{x_j}} + \boldsymbol{e}_3\left(\frac{1}{\tilde{\rho}} - 1\right)\tilde{g} \tag{7}$$

$$\frac{D}{D\tilde{t}}\left[\left(1 + \frac{p_0}{C_v^*\rho_0}\tilde{a_m}\right)\tilde{T} + \frac{p_0}{C_v^*\rho_0}\frac{\tilde{b_m}}{T_0}\right] = \frac{1}{\tilde{\rho}}\frac{\partial}{\partial \tilde{x_j}}\frac{1}{\mathrm{Re}\cdot\mathrm{Pr}}\frac{\partial \tilde{T}}{\partial \tilde{x_j}} \tag{8}$$

$u_i = U\tilde{u_i}$, $\quad T = T_0\tilde{T}$, $\quad \delta p = (U^2\rho_0)\tilde{\delta p}$, $\quad \rho = \rho_0\tilde{\rho}$, $\quad a_m = \tilde{a_m}/\rho_0$, $\quad b_m = \tilde{b_m}/\rho_0$, $\quad x_i = L\tilde{x_i}$, $\quad t = (L/U)\tilde{t}$

$g = (U^2/L)\tilde{g}$, $\quad \mathrm{Re} = \dfrac{UL\rho_0}{\mu}$, $\quad \mathrm{Pr} = \dfrac{\mu}{\kappa/C_v^*}$.

where variables with ˜ are normalized by the characteristic velocity U, length scale L, density ρ_0 and temperature T_0. Hereafter, characters without ˜ denote normalized variables and p represents $\tilde{\delta p}$. C_v^* is regarded as a function of temperature C_v, however, is not affected by the differential operator D/Dt nor $\partial/\partial x_i$. Since μ, κ and C_v change with temperature, Reynolds number Re and Prandtl number Pr are functions of temperature.

The basic equations are solved using the projection method that is a method used in solving the incompressible equations. Using this method, Poisson's equation (9) is derived and solved for obtaining pressure.

$$\mathrm{div}\frac{1}{\rho}\mathrm{grad}p = F + \frac{1}{\Delta t}\left(\mathrm{div}^{*}\boldsymbol{u} - \rho\frac{D^{*}}{Dt}\left(\frac{1}{\rho}\right)\right) \tag{9}$$

$$F = \mathrm{div}\left[-\frac{Du_i}{Dt} + \frac{1}{\rho}\frac{\partial}{\partial x_j}\frac{1}{\mathrm{Re}}\frac{\partial u_i}{\partial x_j} + \boldsymbol{e}_3\left(\frac{1}{\rho} - 1\right)g\right]$$

Operators with $*$ are suitable difference approximations to the original differential operators. The last term with $1/\Delta t$ in Eq. (9) is the correction term used for preventing the accumulation of the error when $\boldsymbol{u}$ is solved using Eq. (7).

The equations are discretized based on the multidirectional finite difference method. Space derivatives are discretized using the second order central difference approximation with the exception of the convective terms. For the convective terms, the third order upwind KK scheme is used to stabilize the computation. It has been found to be the most suitable for the high Reynolds number flow computations. In the third order upwind scheme, the leading numerical error term contains a fourth order derivative, where the effects of the second order numerical diffusions are carefully removed. The numerical diffusion of fourth order derivatives is of short range and does not conceal the effect of molecular diffusion, but at the same time stabilizes the computation.

The second order Crank-Nicolson implicit scheme is used for the time integration.

2.2 The hybrid upwind scheme

In the simulation of the turbulent convective flow at high Reynolds numbers and high temperatures, a high accurate scheme such as the third order upwind scheme is required. In this flow, a temperature gradient becomes very high and the discontinuous surface similar to the shock wave frequently appears in the temperature field. Using the third order upwind KK scheme, the high frequency oscillation caused by the discontinuity can be successfully removed. However, "humps" that appear as an unphysically high or low temperature region are generated near the discontinuous surface. The first order upwind scheme is effective in suppressing such oscillation. However, since the second numerical diffusion contained in the leading numerical error conceals the effect of molecular diffusion, the first order upwind scheme should be used restrictively, only near the discontinuities. In this computation, the hybrid first-third upwind scheme is used for convective terms in the energy equation (8) to remove the oscillations near the discontinuities in the temperature field. In Eq. (10), Adv_3 and Dif_3 represent the advection term and the diffusion term of the convective term approximated by the third order upwind KK scheme. And Dif_1 is the diffusion term from the first order upwind scheme. The hybrid scheme for the x direction in the uniform grid system is given by

$$u\frac{\partial T}{\partial x} \approx Adv_3 + (\alpha \cdot Dif_1 + (1-\alpha)\cdot Dif_3) \tag{10}$$

$$Adv_3 = u_k\frac{-T_{k+2} + 8(T_{k+1} - T_{k-1}) + T_{k-2}}{12\Delta x}, \quad Dif_3 = \frac{|u|\Delta x^3}{4}\cdot\frac{T_{k+2} - 4T_{k+1} + 6T_k - 4T_{k-1} + T_{k-2}}{\Delta x^4}$$

$$Dif_1 = -\frac{|u|\Delta x}{2}\cdot\frac{T_{k+1} - 2T_k + T_{k-1}}{\Delta x^2},$$

where T_k is an approximation of $T(k\Delta x) = T(x_k)$, and α $(0 \le \alpha \le 1)$ in Eq. (10) is the weight for diffusion term from the first order upwind scheme. Weight α is obtained by

$$\alpha = \min\left(1,\ \frac{|D_{xx}\phi_+ + D_{xx}\phi_-|}{4(l_+ + l_-)}\right) \tag{11}$$

$$\phi_{+2} = \phi_{+1} + \frac{T_{k+2} - T_{k+1}}{x_{k+2} - x_{k+1}}, \quad \phi_{+1} = \frac{T_{k+1} - T_k}{x_{k+1} - x_k}, \quad \phi_0 = 0, \quad \phi_{-1} = -\frac{T_k - T_{k-1}}{x_k - x_{k-1}}, \quad \phi_{-2} = \phi_{-1} - \frac{T_{k-1} - T_{k-2}}{x_{k-1} - x_{k-2}}$$

$$l_+ = \sqrt{1^2 + \phi_{+1}^2}, \quad l_- = \sqrt{1^2 + \phi_{-1}^2}, \quad D_{xx}\phi_+ = \frac{\phi_{+2} - 2\phi_{+1} + \phi_0}{2}, \quad D_{xx}\phi_- = \frac{\phi_0 - 2\phi_{-1} + \phi_{-2}}{2}.$$

$T \mapsto \phi$ at each grid point is a temperature gradient preserving map (Fig. 1). $D_{xx}\phi_+$ represents the difference between ϕ_{+1} and the average of ϕ_{+2} and ϕ_0. Similarly, $D_{xx}\phi_-$ is the difference between ϕ_{-1} and the average of ϕ_0 and ϕ_{-2}. $l_+ + l_-$ is the sum of two sides of triangle $\phi_{+1}\phi_0\phi_{-1}$. They are explained in Fig. 2. Weight α represents the discontinuity at the next points of the temperature curve.

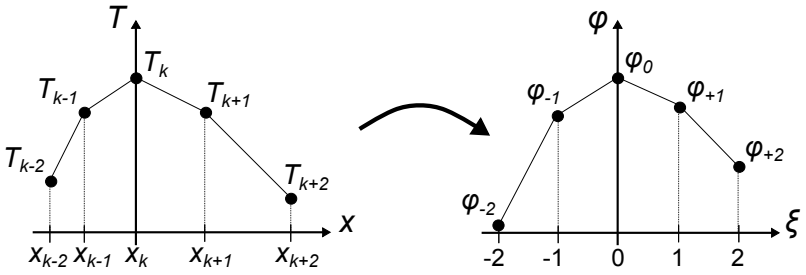

Figure 1: Temperature-gradient preserving map $T \mapsto \phi$.

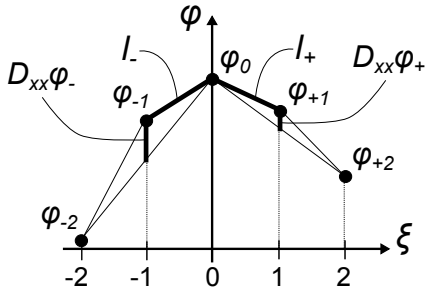

Figure 2: Geometric meaning of weight α.

On the other hand, Dif_3 that contains the difference approximation of the fourth order derivative, is rewritten as

$$Dif_3 = \frac{|u|}{\Delta x} \cdot \frac{D_{xx}T_+ - 2D_{xx}T_0 + D_{xx}T_-}{2} \tag{12}$$

where

$$D_{xx}T_+ = \frac{T_{k+2} - 2T_{k+1} + T_k}{2}, \quad D_{xx}T_0 = \frac{T_{k+1} - 2T_k + T_{k-1}}{2}, \quad D_{xx}T_- = \frac{T_k - 2T_{k-1} + T_{k-2}}{2}.$$

Equation (12) (and Fig. 3) shows that a diffusion effect of Dif_3 can work at the central point when the strong discontinuity appears either at the central point or at one of the next points. This is the reason of generating "humps" using the third order upwind scheme.

When the strong discontinuity appears only at the neighboring points and not at the central point, α becomes large suppressing the effect of Dif_3, while Dif_1 becomes effective at the central point. However, because the discontinuity at the central point is small, the value of Dif_1 that consists of the second diffusion should also be small, and the overabundant diffusion effects due to the first order upwind scheme can be avoided.

On the other hand, when a strong discontinuity appears only at the central point, α becomes small and the high frequency oscillation at the discontinuous point is removed by Dif_3 that is the effect of the third order upwind scheme.

It should be noted that, in the present hybrid scheme, the first order upwind scheme is employed for the purpose of preventing the oscillation not to remove the oscillation that is already present.

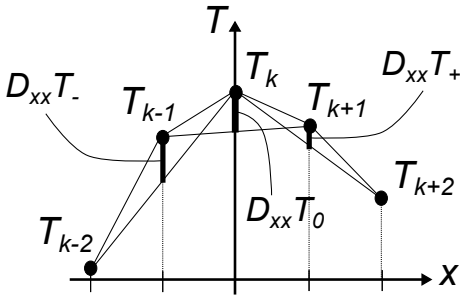

Figure 3: Geometric meaning of Dif_3.

2.3 Boundary conditions

The geothermally heated water issues from a hydrothermal vent in the deep sea, while the cold sea water is absorbed into the seafloor. That can be called "seafloor hydrothermal circulation", and large amount of water is always stored within the oceanic crust. Since the seafloor hydrothermal circulation is the very large-scale system, too much computer resources are required to simulate the hydrothermal convection of the whole seafloor hydrothermal circulation. In the present computation, the flow is assumed to be axisymmetric about the x_3 axis that passes through the center of the circular vent (Fig. 4). The radius of the vent is h =2.5 cm and a heated water pool is placed under seafloor with a partition-wall dividing the domain. The flow simulation is carried out in the x_1x_3 domain using a non-uniform Cartesian grid that is concentrated near the hydrothermal vent. The number of grid points is 513 × 513.

A convection condition at the top boundary and a zero gradient condition at the side boundary are employed for the velocity and temperature. At the bottom, free-slip boundary condition is imposed. The heated water pool and the sea above the seafloor are partitioned by a non-slip and non-thermal-conduction wall. The temperature of the wall is the same as the initial temperature of the ambient water.

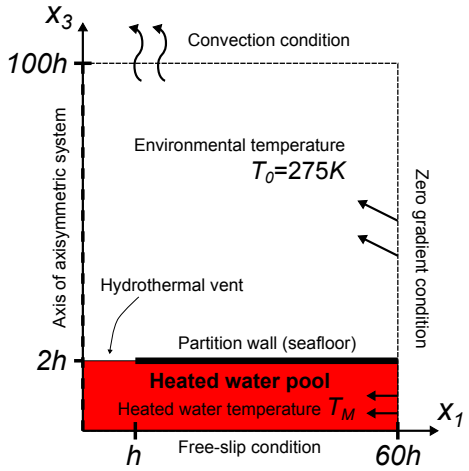

Figure 4: Computational domain in the axisymmetric system about the x_3 axis.

3 Computational Results

Flow simulations for hydrothermal convection are carried out for two cases of temperature $T_M = 625$ K and 675 K, both near the critical temperature 647.096 K. The pressure and temperature of the environmental water are 23 MPa and 275 K respectively. In the case of $T_M = 625$ K, the heated water is in the liquid state because the temperature is lower than the critical temperature (Fig. 5 and Table 1). On the other hand, the heated water at 675 K is in the supercritical state, while it becomes liquid when cooled down.

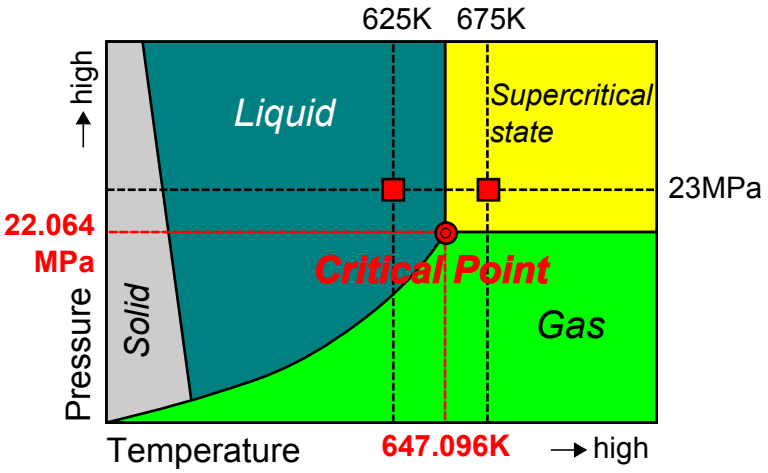

Figure 5: Water pressure-temperature phase diagram.

Table 1: Critical properties of water.

Temperature	647.096 K
Pressure	22.064 MPa
Density	322 kg/m^3

How the physical properties and non-dimensional parameters change with water temperature when the pressure is constant at 23 MPa, are presented in Fig. 6. Figure 6 shows they significantly change near the critical temperature of 647.096 K.

Figures 7 and 8 show the temperature fields at the initial stages of computation for the $T_M = 625$ K and 675 K cases. The black line in Fig. 8 is the contour line representing the critical temperature. In the same way, Figs. 9 - 16 show the initial stages of the density, Reynolds number, Prandtl number and Grashof number fields. The Reynolds number and the Grashof number are defined by the diameter of the vent and the average spouting velocity at the vent. The convective flow of the $T_M = 675$ K case shows more fluctuations

and develops faster than the $T_M = 625$ K case. Also in the $T_M = 675$ K case, the Reynolds number, Prandtl number and Grashof number significantly change in the flow field. It suggests that the flow is much more complicated containing several different fluid dynamic characteristics, because the temperature is changing near the critical temperature for the $T_M = 675$ K case.

In Figs.17 and 18, the time averaged fields of temperature and vertical velocity are presented for each case of T_M. The physical properties are time averaged between 2 s and 6.5 s. By comparing the figures, it can be found that in the $T_M = 675$ K case the flow near the vent is fluctuating more. Also a localized flow going down next to the upward flow can be found.

Figure 19 shows time development of the flow field between 3.35 s and 3.62 s for the $T_M = 675$ K case. In this figure, time-series-images are displayed from the bottom to the top and from the left to the right. In each image, vertical velocity field with black contour line representing the critical temperature (inversion image) and the time derivative of baroclinic torque $-(g/\rho)\partial\rho/\partial x_1$ are presented on the left and right sides, respectively. The figure shows large unsteady and fast change of the over-critical-temperature region. On the outerside, vortex-pairs moving downward by self-induced velocities can be found. That can be the reason for the downwash found in the time averaged field.

The visualization software used here is Clef2D developed by Institute of Computational Fluid Dynamics.

4 Conclusions

Hydrothermal convective flows of two temperatures near the critical temperature were simulated using the numerical method similar to an incompressible flow. Under conditions close to the critical temperature, the flow was sensitive to the temperature of the heated water and large difference in the flow field was observed. At temperature above the critical temperature at 675 K, the thermal convection developed faster and explosively. Also in this case, the flow structure was extremely complex and unsteady. The phenomenon may be because the density and other physical properties change significantly even with small changes in the temperature, when the temperature is near the critical temperature. In the convective flow near the critical temperature, if some part of the flow field's temperature is above the critical temperature, the fluid dynamic characteristics of the flow can be significantly different.

5 Acknowledgments

The author is grateful to Professor J. Kim for his help in carrying out the numerical simulation. This work was partially supported by Grant-in-Aid for Scientific Research from MEXT/JSPS (22740261).

References

[1] T. Kawamura and K. Kuwahara. Computation of high Reynolds number flow around a circular cylinder with surface roughness. *AIAA paper*, 84-0340, 1984.

[2] S. Komurasaki, T. Kawamura and K. Kuwahara. Simulation of thermal convection in a stratified fluid flow. *AIAA paper*, 2002-0877, 2002.

[3] K. Kuwahara. Computation of thermal convection with a large temperature difference. *Proc. Int. Conf. on Applied Numerical Modeling*, 1984.

[4] Y. X. Ren, M. Liu and H. Zhang. A characteristic-wise hybrid compact-WENO scheme for solving hyperbolic conservation laws. *J. Comp. Phys.*, 192:365-386, 2003.

[5] H. Suito, K. Ishii and K. Kuwahara. Simulation of Dynamic Stall by Multi-Directional Finite Difference Method. *AIAA paper*, 95-2264, 1995.

[6] H. Takami and K. Kuwahara. Numerical Study of Three-Dimensional Flow within a Cubic Cavity. *J. Phys. Soc. Jpn.*, 37:1695, 1974.

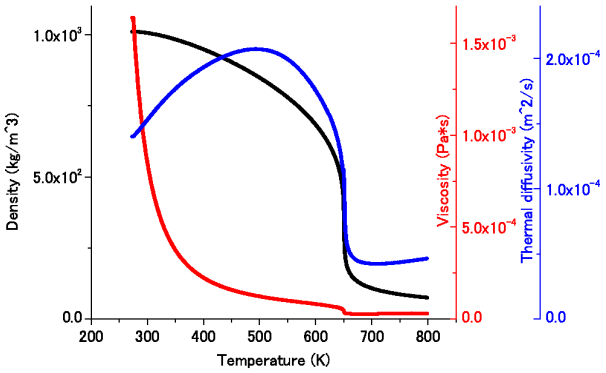

(a) Density ρ (black), viscosity μ (red) and thermal diffusivity κ/C_v (blue).

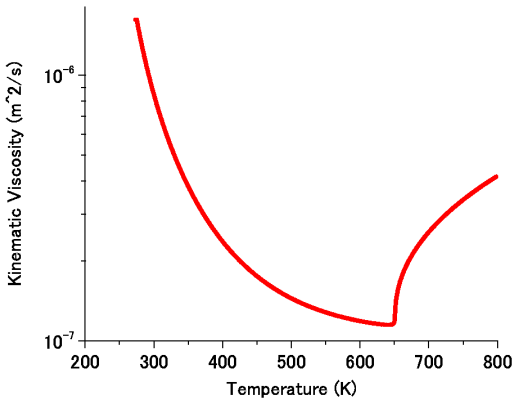

(b) Kinematic viscosity $\nu = \mu/\rho$.

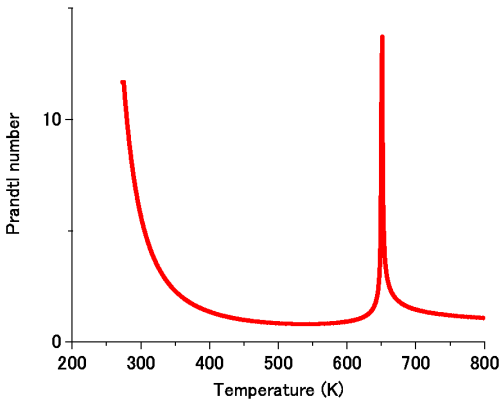

(c) Prandtl number Pr.

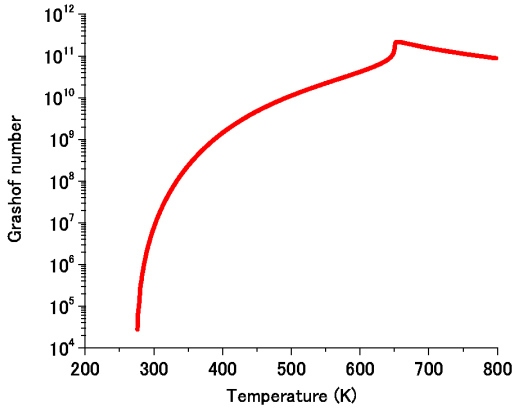

(d) Grashof number Gr based on the diameter of the vent $2h$ and the environmental temperature T_0.

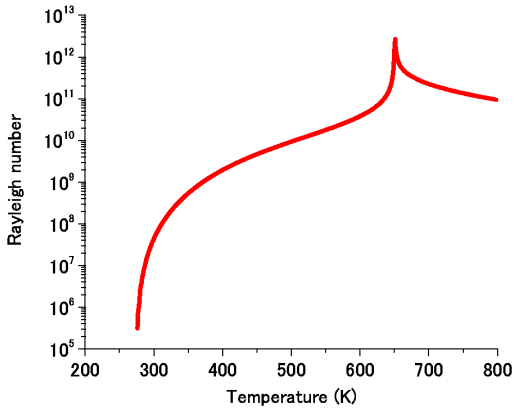

(e) Rayleigh number Ra.

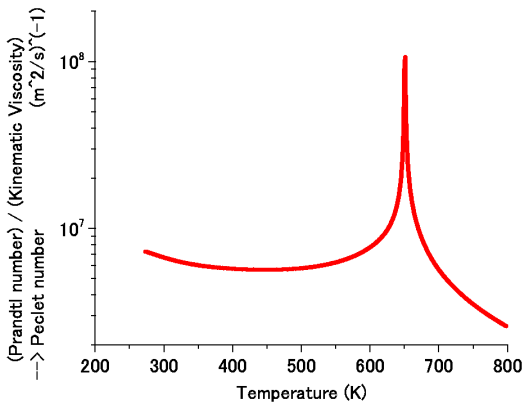

(f) (Prandtl number)/(Kinematic viscosity) $\rightarrow$ Peclet number Pe.

Figure 6: Physical properties and non-dimensional parameters depending on temperature for water at pressure of 23MPa.

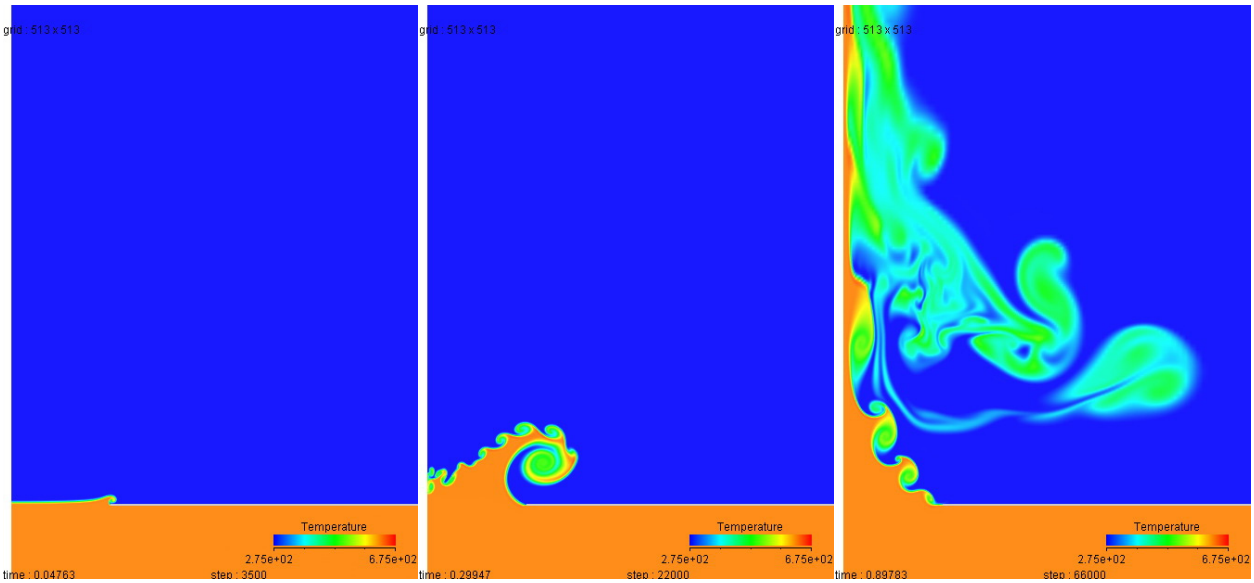

$t = 0.05$ s $t = 0.3$ s $t = 0.9$ s

Figure 7: Temperature fields at initial stages for the T_M =625 K case. Temperature shading in the range 275 K - 675 K.

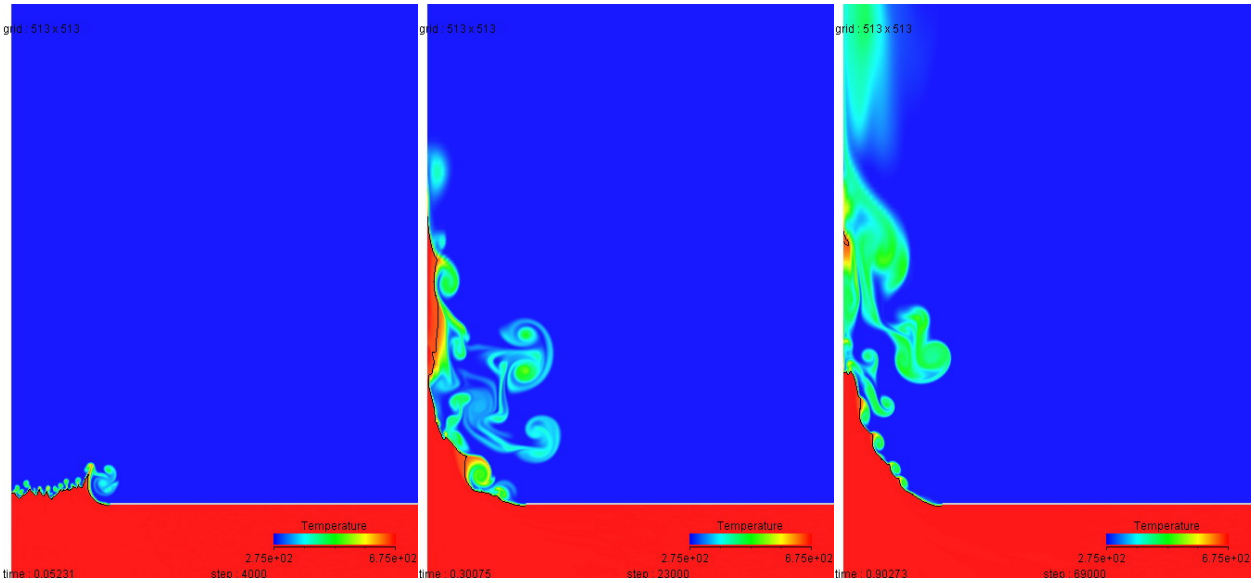

$t = 0.05$ s $t = 0.3$ s $t = 0.9$ s

Figure 8: Temperature fields at initial stages for the T_M =675 K case. Temperature shading in the range 275 K - 675 K. Black contour line representing the critical temperature.

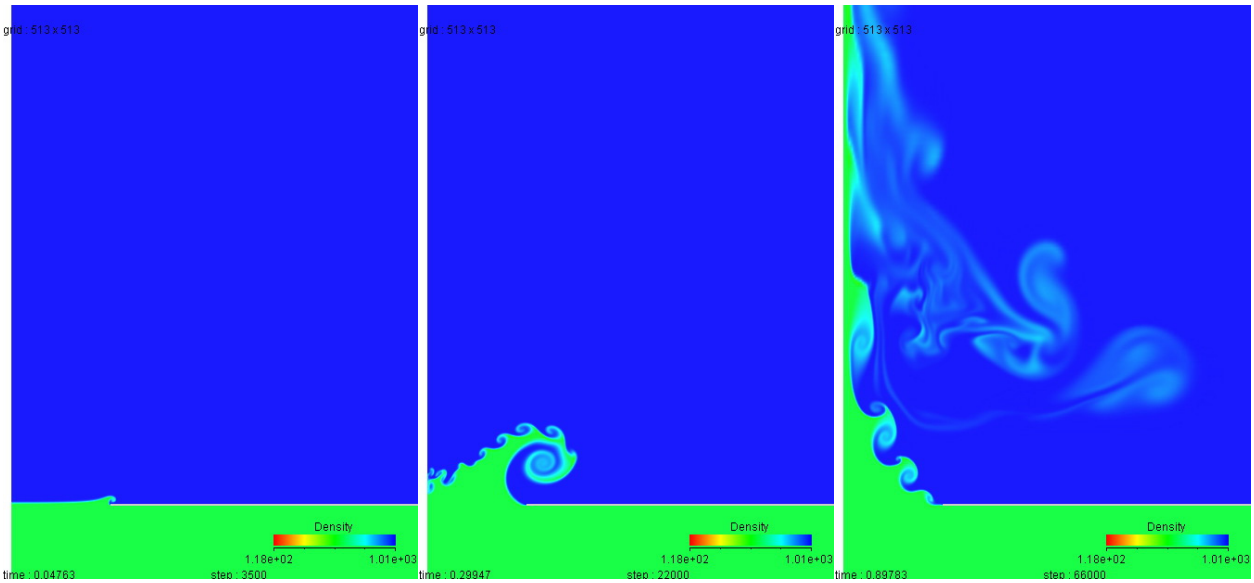

$t = 0.05$ s $t = 0.3$ s $t = 0.9$ s

Figure 9: Density fields at initial stages for the T_M =625 K case. Density shading in the range 118 kg/m^3 - 1011 kg/m^3.

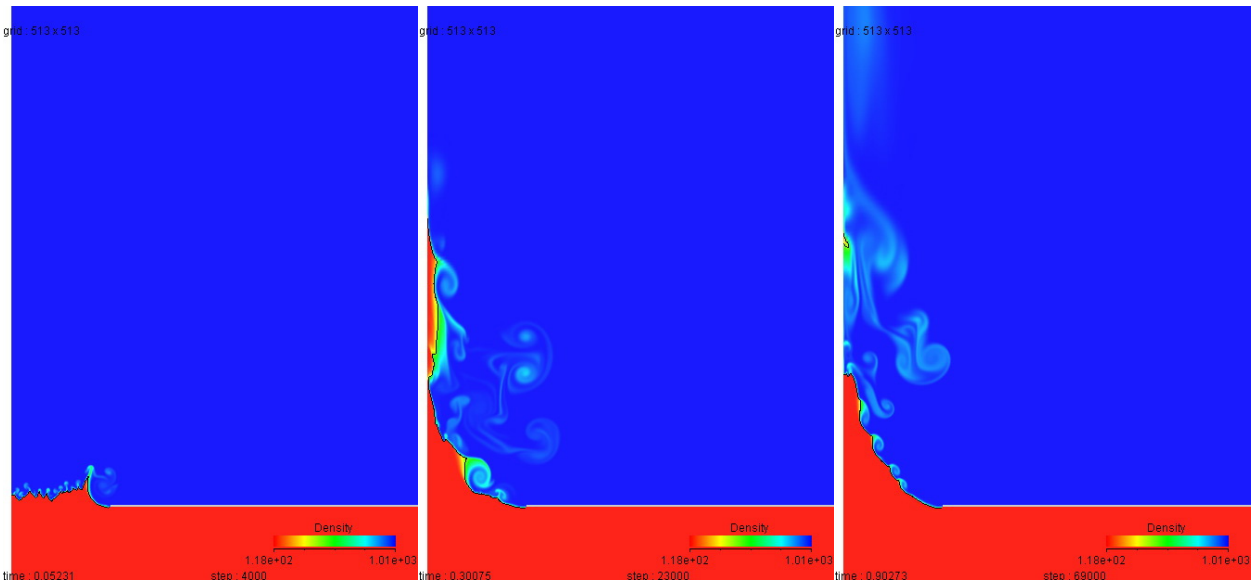

$t = 0.05$ s $t = 0.3$ s $t = 0.9$ s

Figure 10: Density fields at initial stages for the T_M =675 K case. Density shading in the range 118 kg/m^3 - 1011 kg/m^3. Black contour line representing the critical temperature.

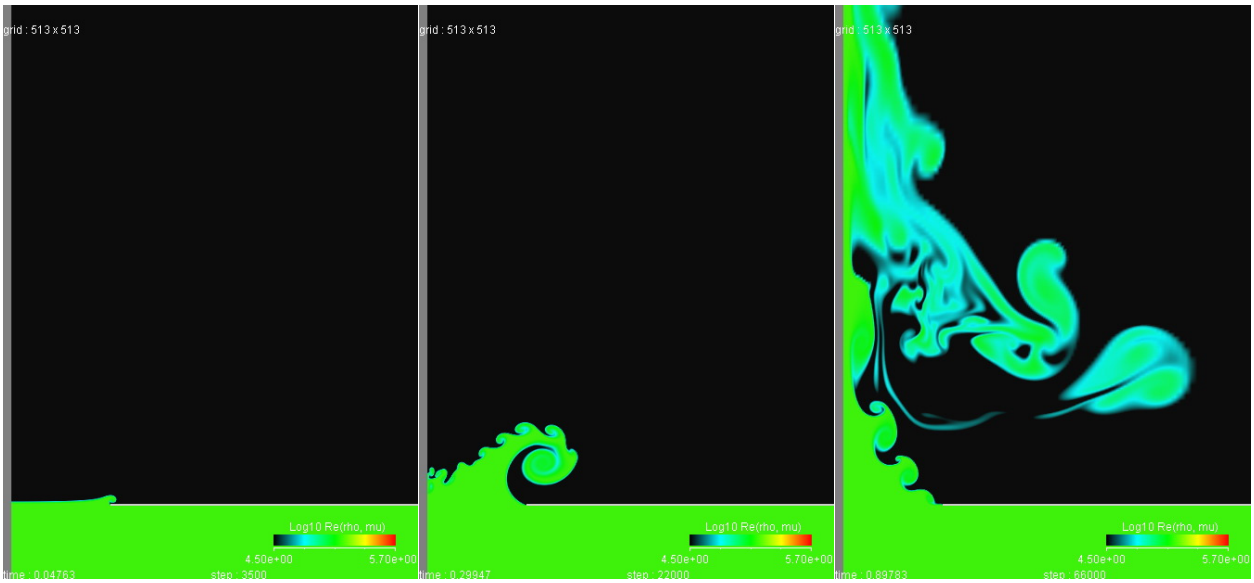

$t = 0.05$ s $t = 0.3$ s $t = 0.9$ s

Figure 11: $\log_{10}$Re in the flow fields at initial stages for the T_M =625 K case. Color shading in the range 4.5 - 5.7.

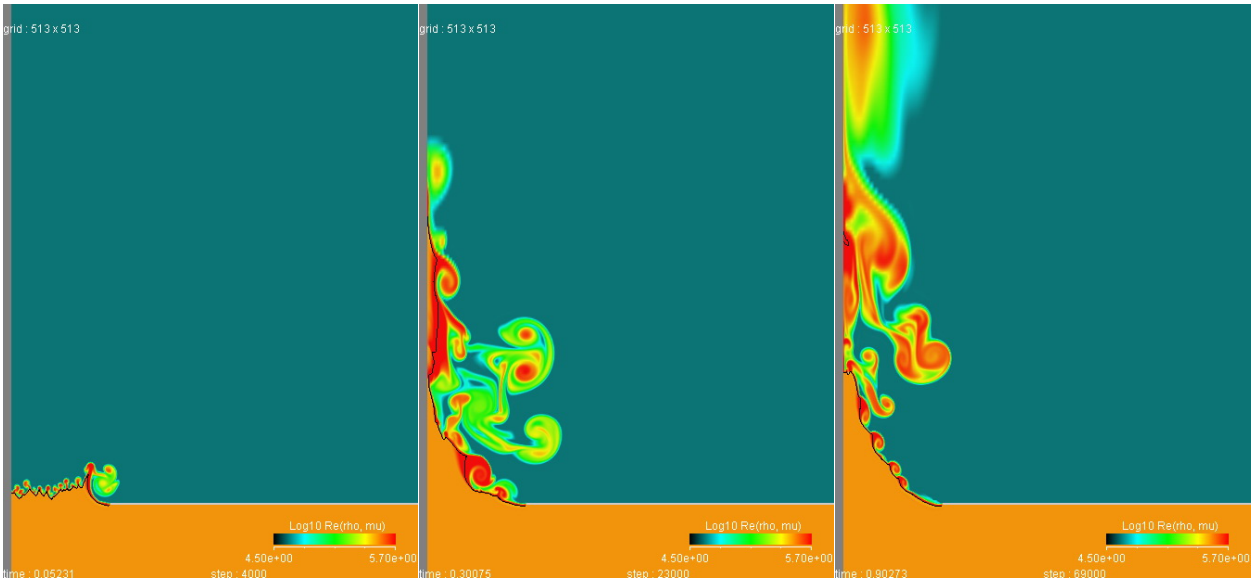

$t = 0.05$ s $t = 0.3$ s $t = 0.9$ s

Figure 12: $\log_{10}$Re in the flow fields at initial stages for the T_M =675 K case. Color shading in the range 4.5 - 5.7. Black contour line representing the critical temperature.

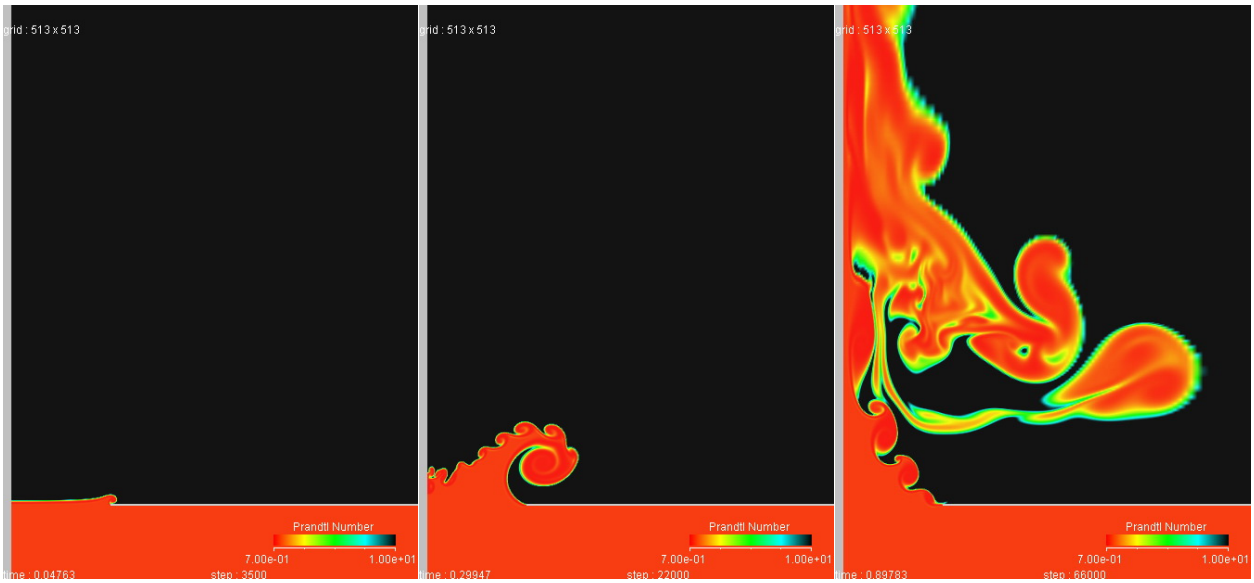

$t = 0.05$ s $t = 0.3$ s $t = 0.9$ s

Figure 13: Prandtl numbers in the flow fields at initial stages for the T_M =625 K case. Color shading in the range 0.7 - 10.

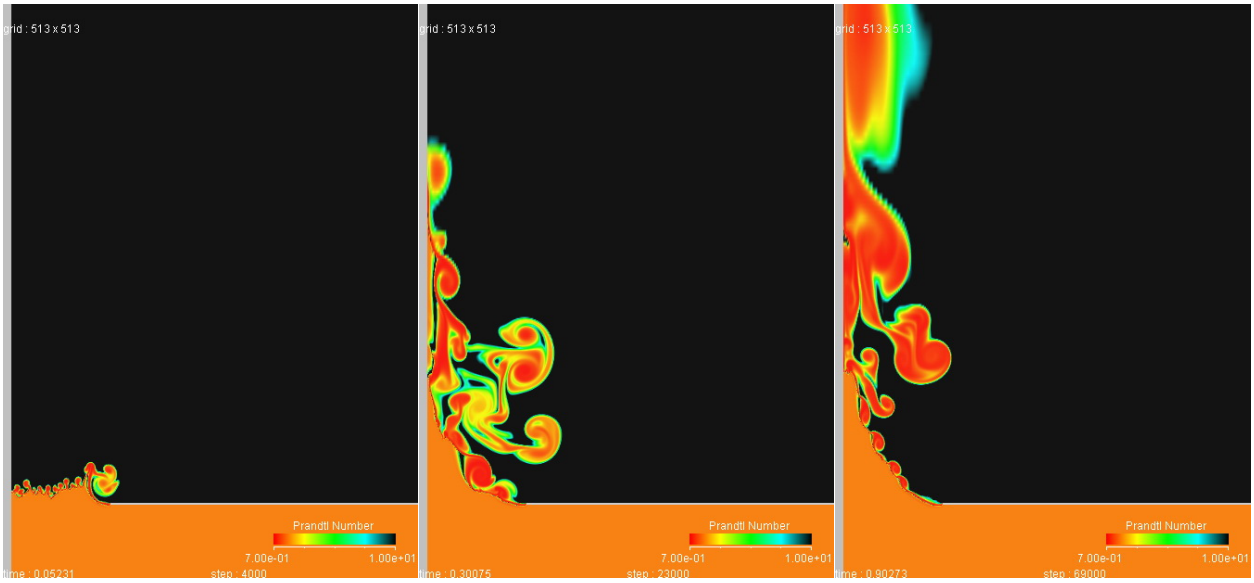

$t = 0.05$ s $t = 0.3$ s $t = 0.9$ s

Figure 14: Prandtl numbers in the flow fields at initial stages for the T_M =675 K case. Color shading in the range 0.7 - 10.

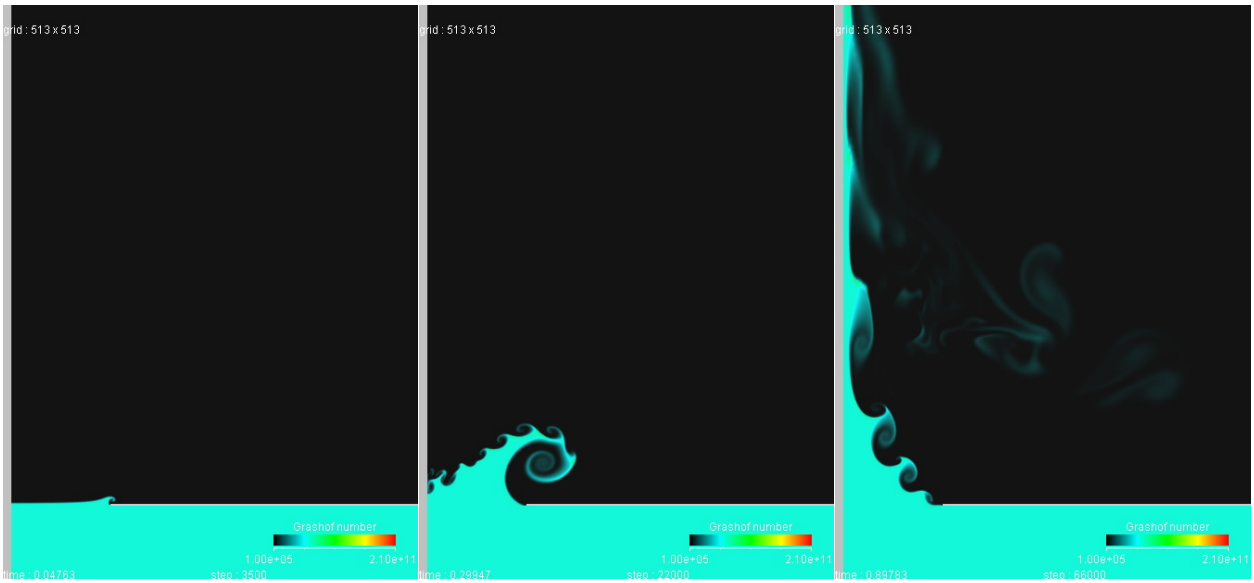

$t = 0.05$ s $t = 0.3$ s $t = 0.9$ s

Figure 15: Grashof numbers in the flow fields at initial stages for the T_M =625 K case. Color shading in the range 10^5 - 2.1×10^{11}.

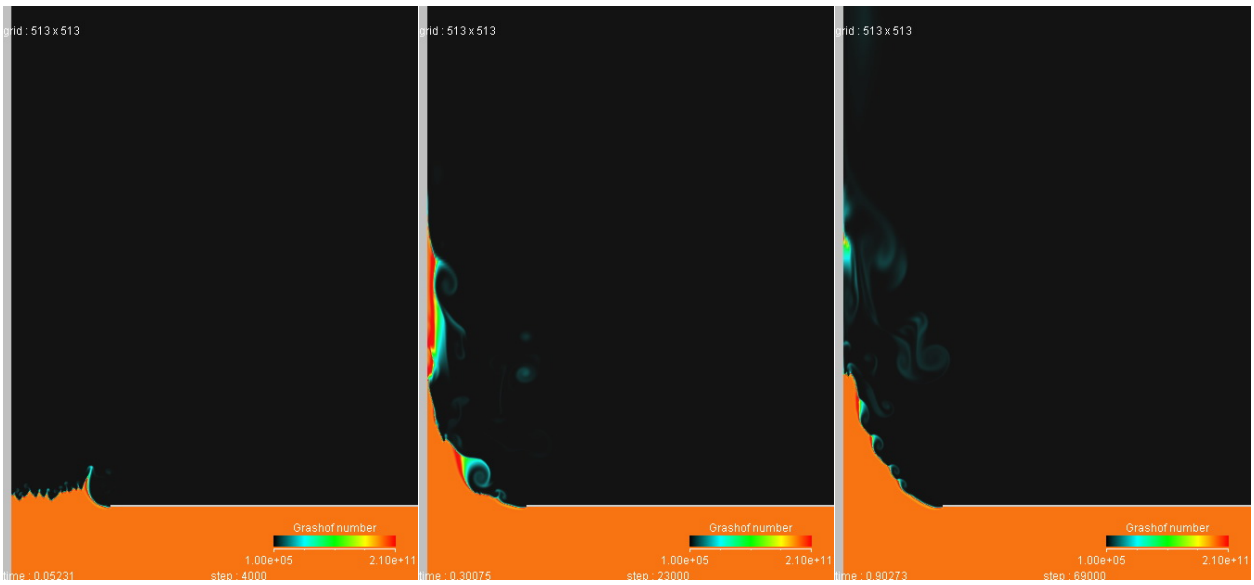

$t = 0.05$ s $t = 0.3$ s $t = 0.9$ s

Figure 16: Grashof numbers in the flow fields at initial stages for the T_M =675 K case. Color shading in the range 10^5 - 2.1×10^{11}.

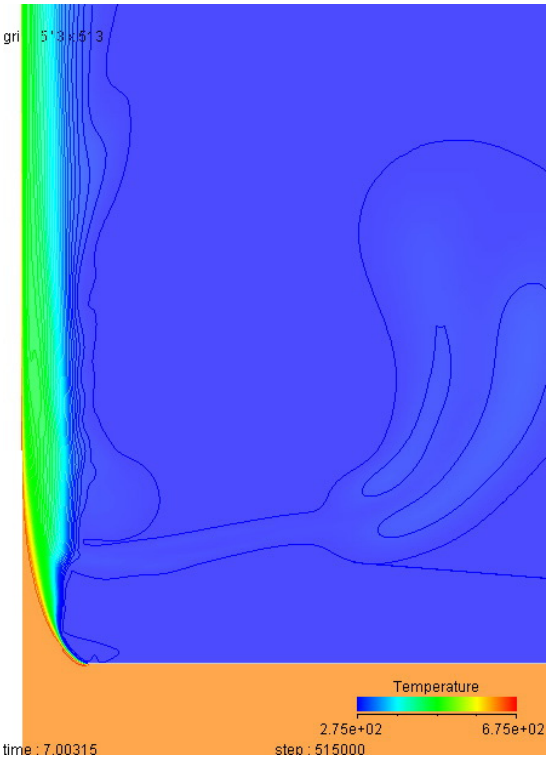

$T_M = 625$ K

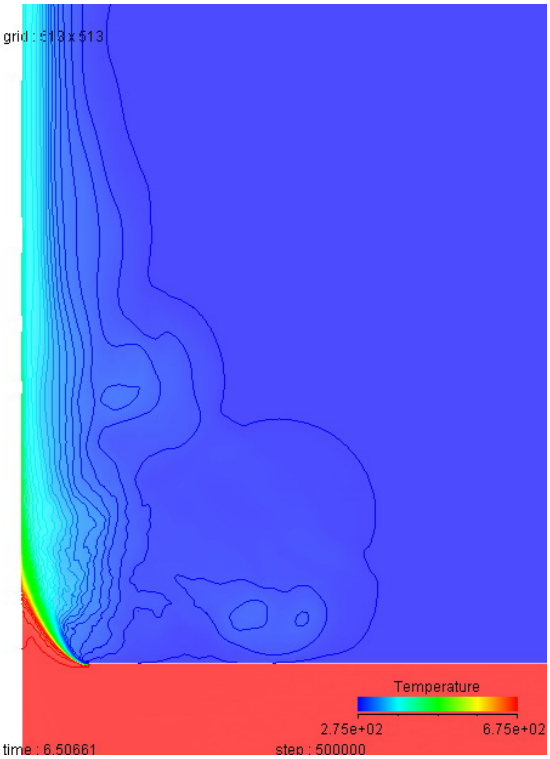

$T_M = 675$ K

Figure 17: Time averaged temperature fields. Temperature shading and contour lines in the range 275 K - 675 K.

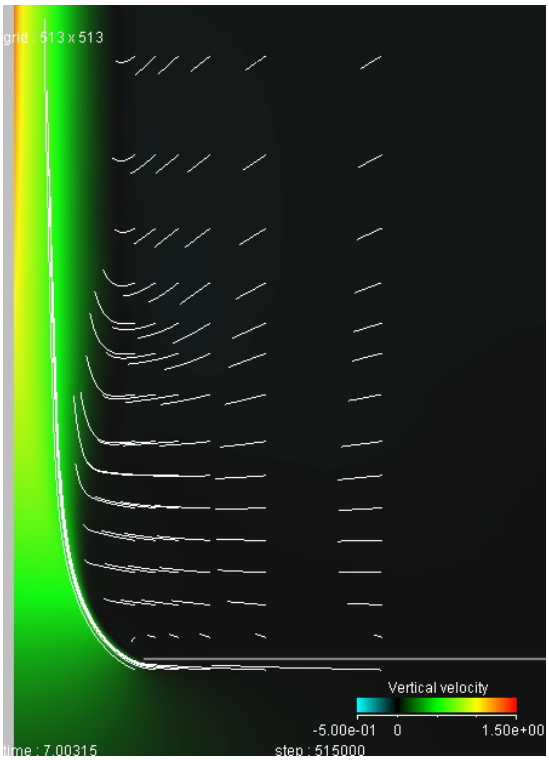

$T_M = 625$ K

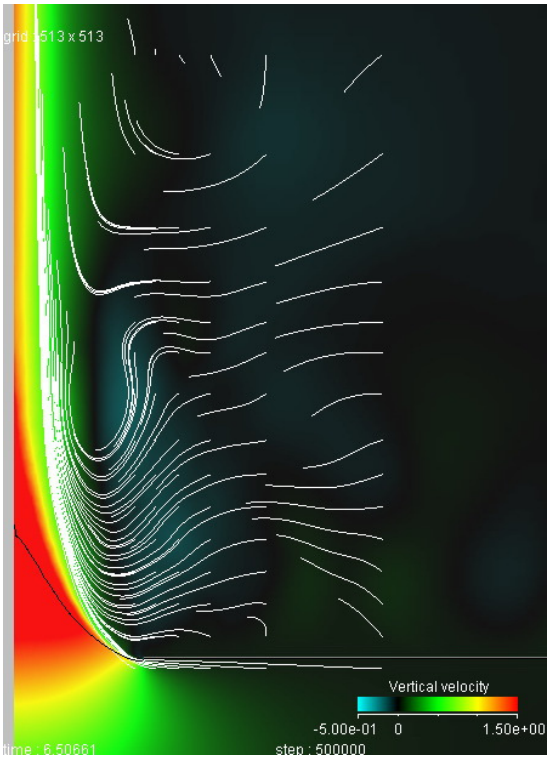

$T_M = 675$ K (Black line : the critical temperature)

Figure 18: Vertical velocity and stream lines in the time averaged fields. Vertical velocity shading in the range -0.5 - 0 - 1.5 m/s (blue - black - red).

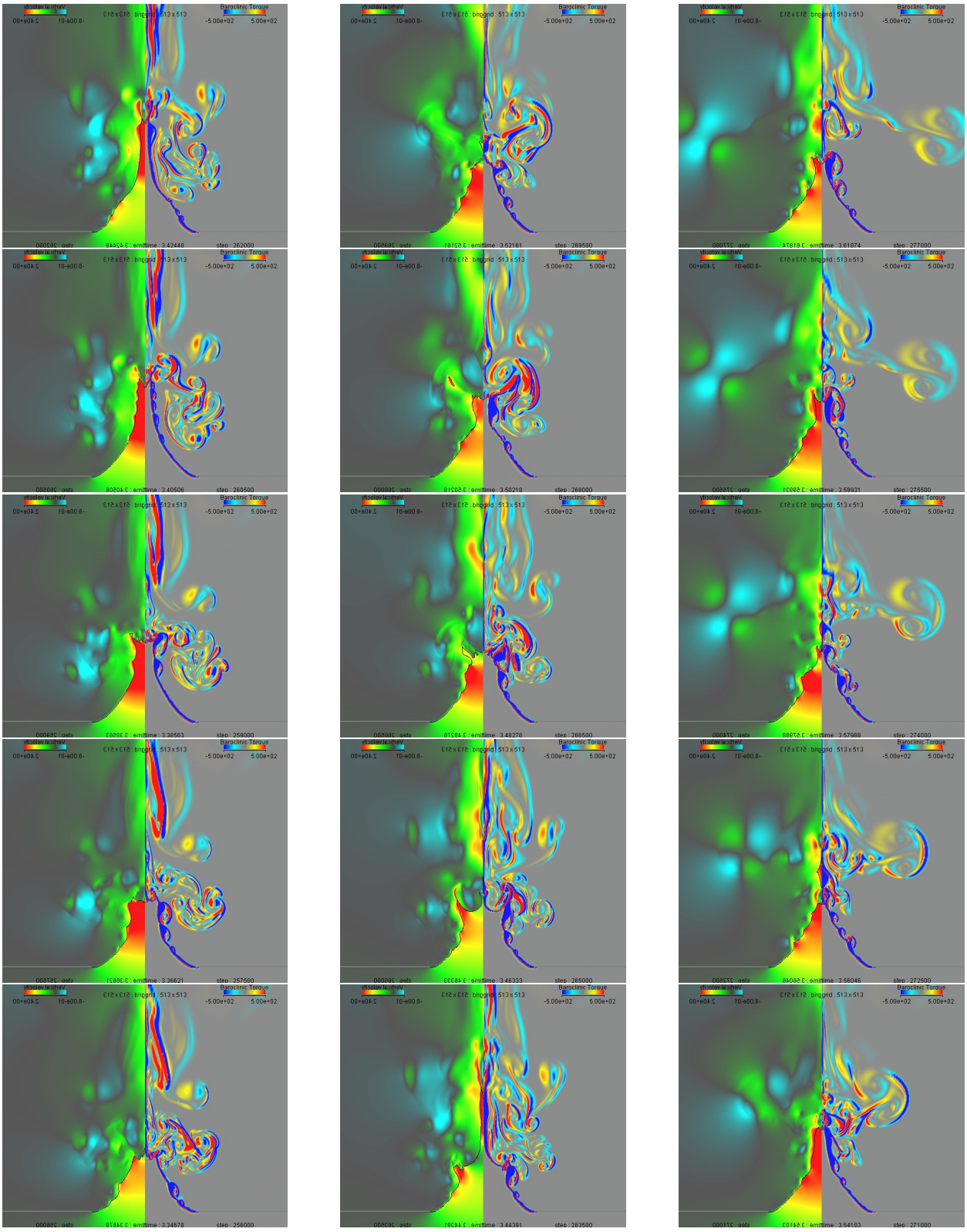

Figure 19: Time development of the flow field in the T_M =675 K case. Time sequence: from the bottom to the top and from the left to the right. Left of the vertical axis: vertical velocity shading (inversion image) in the range −0.8 - 0 - 2.4 m/s (blue - gray - red). Black contour line representing the critical temperature. Right of the vertical axis: Time derivative of baroclinic torque. Color shading: red-counterclockwise and blue-clockwise.